Automated Optimization of the MULDICON Inlet with Minimum Losses and Reduced Sight onto the Compressor Front Face

Christian Voß*, Marco Trost† and Richard G. Becker‡
German Aerospace Center (DLR), Cologne, Germany, D-51147

The main target of the DLR project Mephisto is to achieve a holistic design capability for a UCAV configuration in military use. In order to ensure survivability of the aircraft a reduction of the visibility of the fan area for preventing radar and infrared detection is necessary. In addition, the flow losses should be kept as low as possible and a homogeneous inflow to the engine should be achieved. Therefore, an S-shaped engine intake duct is designed via automated optimization. Within this optimization process 27 free geometrical parameters are varied to design the intake duct, considering aerodynamic flow field characteristics.

The optimized S-duct geometries show a significant visibility reduction onto the engine compressor unit, with tolerable total pressure losses and acceptable flow inhomogeneities.

I. Nomenclature

AIP	=	aerodynamic interface plane
CFD	=	computational fluid dynamics
CSM	=	computational structure mechanics
$DC60$	=	distortion coefficient
DOE	=	design of experiments
EVG	=	expected volume gain
f	=	objective
Ma	=	Mach number
MM	=	metamodel
p_t	=	total pressure
$SC60$	=	swirl distortion coefficient
u	=	axial flow velocity
$UCAV$	=	unmanned combat aerial vehicle
UDP	=	user defined process chain
V	=	visibility
VG	=	volume gain
y^+	=	dimensionless wall distance
π	=	total pressure coefficient
τ_w	=	wall shear stress
φ	=	circumferential angle
ω	=	total pressure loss coefficient

II. Introduction

For military applications, aircraft must be able to act quickly, flexibly and undetected. Thus, special demands exist on design, external aerodynamics and agility [1]. Especially for the use of military aircraft operating at subsonic speed in hazardous areas, the use of stealth technology is essential. Within the scope of this technology, flat-shaped UCAV

*Research Scientist, Institute of Propulsion Technology, German Aerospace Center (DLR), Cologne, Germany, 51147.
†Research Scientist, Institute of Propulsion Technology, German Aerospace Center (DLR), Cologne, Germany, 51147.
‡Research Scientist, Institute of Propulsion Technology, German Aerospace Center (DLR), Cologne, Germany, 51147.

configurations are used to reduce the number of sharp edges in order to reduce the radar signature. With this technology and the support of shielding materials, a detection by radar or infrared measurements can be almost avoided [2],[3].

In addition to the external shape of an aircraft, the visibility of the fan has a significant effect on the aircrafts detectability. Due to the high-frequency rotation of the fan blades and its sharp edges of the fan blades, shielding materials are insufficient to reduce the radar signature. A solution for this problem is the geometric adjustment of the intake in front of the fan [3]. The design of a long, curved intake, known as an S-duct, can reduce or even avoid visibility to the fan. However, for the effective operation of an engine, homogeneous inflow to the fan is essential and the formation of secondary flow areas by flow separation or vortex formation must be avoided [4].

The presented paper deals with the computer-aided design of an S-shaped intake for the UCAV configuration created in the DLR project Mephisto [5]. For these investigations the automated optimizer *AutoOpti* is used, which needs an automated process chain for S-duct generation and meshing followed by 3D CFD and post-processing. The optimization objectives and constraints must take visibility at the aerodynamic interface plane (AIP), flow losses and homogeneity into account. The automated calculation of the internal flow is realized by the 3D flow solver TRACE [6]. All necessary boundary conditions of the external flow as well as the boundary conditions at the compressor intake are provided from previous performance calculations. The final numerical solutions will be used to evaluate the most promising optimized S-ducts in terms of fluid mechanical losses and signature reduction. Based on these results, a final design decision is made.

III. Optimization Setup

A. *AutoOpti*

In this study the parallelized, multiobjective, metamodel assisted framework *AutoOpti* is used which is developed at the DLR Institute of Propulsion Technology since 2002 ([7],[8],[9],[10],[11],[12]). Fig. 1 shows the basic flowchart of the optimizer. An optimization consists of one master-process (grey/blue in Fig. 1), which handles the optimization algorithms, and several slave processes (yellow in Fig. 1) which are responsible for the specific user defined process chain (notation: UDP). In order to calculate the objective/constraint values of a member (note: a member is defined as a given set of free variable of the optimization problem), the master process hands over a member to a slave process and, upon termination, receives its simulation results (e.g.: CFD/CSM). With these results the objective functions and constraints can be calculated and the member is ranked and stored in the database. Afterwards the Pareto rank is updated for all stored members.

In the next step the master process creates a new more or less auspicious member:

- In case of simple evolutionary creation, some members (notation: parents) are selected from the database based on their Pareto rank and several parents are recombined, using different but quite simple and fast operators like Mutation, Differential Evolution, and Crossover to produce an offspring.
- In case of creation via metamodels (notation: MM), the metamodels for all relevant values are trained and a temporary optimization is performed which searches for a member with the highest expected volume gain (notation: EVG, see [11],[12]) or volume gain (notation VG: see below) with respect to the current Pareto front and the currently evaluated members of all running slave processes. As metamodels Kriging (ordinary Kriging, Co-Kriging for multi-fidelity optimization's and gradient enhanced Kriging for optimizations using adjoint solvers) and artificial neural networks are available in *AutoOpti*. Finally the new member is sent to the free slave and the previously described master/slave cycle is run again until the optimizations convergence criteria are reached or the user aborts the program.

In the presented investigation first a design of experiments (DOE) was performed, and afterwards most of the members were created using the embedded MM-strategy described above by using ordinary kriging models. As explained in detail in [11] the objective during the temporary optimization on the MM is the EVG criterion by default, which needs beside the kriging forecast of the expectation values also the kriging variances as a measure of uncertainty. This procedure may become a bottle neck of the optimization if the UDP is quite fast and the database becomes large. Therefore a new procedure called volume gain (VG) is implemented to *AutoOpti* which just needs the expectation values of the metamodels and therefore avoids the time consuming calculation of the variances. In the presented study a mixture between EVG, VG and simple evolutionary operators was used to balance the numerical effort between master- and slave-processes.

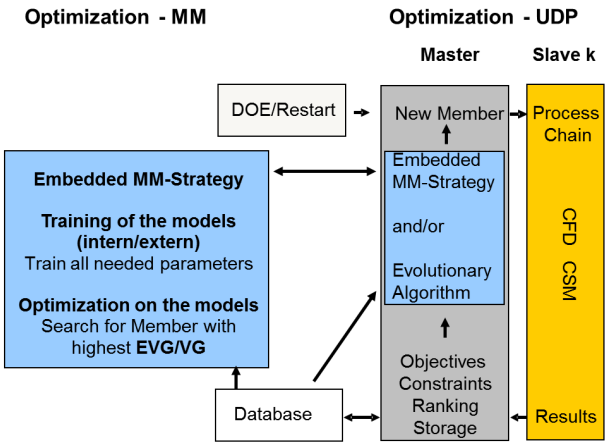

Fig. 1 Flowchart *AutoOpti*.

B. Geometry creation and visibility rating

For designing the S-duct geometry the DLR developed software "DuctGen" is used. DuctGen creates a "spine"-curve in three dimensional space, on which any number of "rib"-curves can be placed as explained in [13]. As seen in Fig. 2 (right), there are direction vectors which are used to determine the three-dimensional progression of the spine-curve at the inlet and outlet of the S-duct. Between these, the spine-curve is parameterized by 3D points which are interpolated.

The rib-curves placed along the spine-curve are parameterized by the specification of control points in a two-dimensional cartesian coordinate system or by polar coordinates. Symmetries can be imposed to the rib curves to reduce free parameters and to ensure geometric constraints. Additionally the ribs can be rotated around the origin of the coordinate system. The 2D rib-curves are transformed to 3D by user defined positioning on the spine curve and the finale S-duct is created by a surface skinning procedure (see Fig. 2).

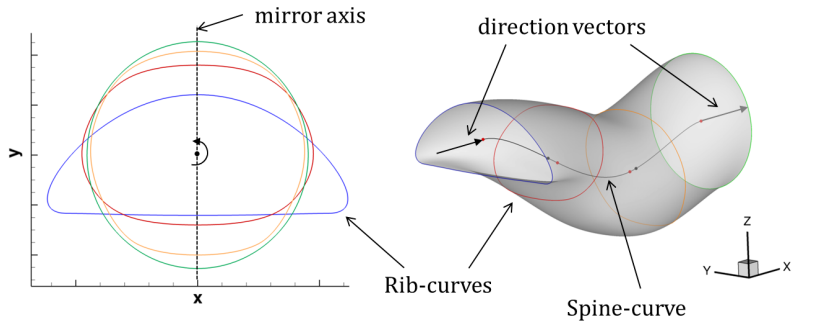

Fig. 2 Generated S-duct geometry (right) with DuctGen by single rib-curves (left).

The visibility is calculated by the visibility-tool developed at DLR. It enables the determination of the visible area of the S-duct outlet as a relative quantity, which can be used as an objective in the optimization process.

With this tool the relative visible area of the S-duct outlet panel seen from the inlet panel is checked. By linear connecting any point of the S-duct entry surface with all points of the outlet panel, the number of visible points on the outlet panel is determined. These visible points are all outlet points that have a linear connection to an inlet point without intersecting the S-duct surface, as shown in Fig. 3. Accordingly, the value of visibility V is defined as the ratio of visible points D_{vis} in the outlet panel to all points D_{total} in the outlet panel:

$$V = \frac{D_{vis}}{D_{total}}. \tag{1}$$

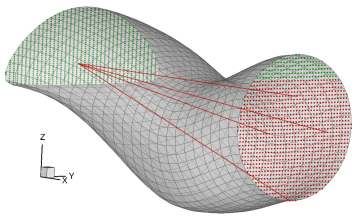

Fig. 3 Principle of the visibility check.

C. Mesh

Within DuctGen a structured multi-block grid is generated [13]. The mesh has a butterfly topology and the different blocks of the mesh are arranged in an H-structure. Moreover DuctGen gives the possibility to divide the duct in several block segments and to set different mesh parameters in each block segment. This ensures a high convergence rate during the optimization process.

The grid used for optimization is shown in Fig. 4. This grid has an entry block, a center block and an exit block. For parallelization and a resulting acceleration of the CFD flow simulation all blocks are splitted into smaller blocks. Further input settings are the options to control the H-block structure, the block edges and the size of the first wall distance.

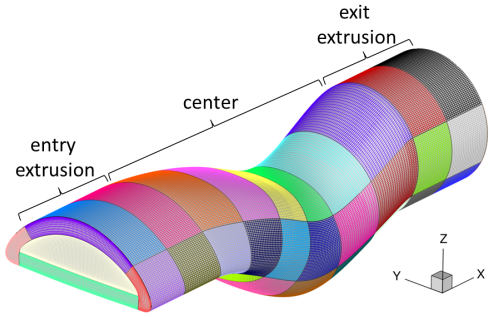

Fig. 4 Structured volume mesh of the S-duct.

D. Flow solver and boundary conditions

For CFD flow simulation the flow solver TRACE 9.0 is used, which is developed by the Institute of Propulsion Technology of the DLR in cooperation with MTU Aero Engines. With TRACE, both stationary and transient states of flows in axial and radial turbomachinery components can be calculated. For this the Reynolds averaged Navier-Stokes equations are discretized using the finite volume method. For closing unknown turbulent terms the two equation k-ω model by Wilcox is used in the presented investigations [14]. Stationary CFD configurations are performed with fully turbulent flow.

A homogeneous and parallel inflow state is assumed. The influence of the spinner at the compressor inlet is neglected. In addition, the boundary layer thickness formed by the aircraft structure in front of the intake duct is not considered. A dimensionless wall distance of $y^+ \simeq 1$ is achieved by the mesh generating process.

For running the CFD simulation the total pressure and total temperature as well as turbulence parameters for the k-ω model are set at the inflow using a Riemann boundary condition. Therefore the inlet boundary conditions were calculated in previous performance calculations with the inflow Mach number $Ma = 0,8$ at the design point “cruise”. At this operation point the ambient conditions are calculated at flying altitude of $11000\,m$ at standard atmosphere conditions. To ensure efficient operation of the compressor a constant mass flow ratio for all generated ducts is required.

E. Process chain

The implemented process chain in *AutoOpti* is shown in Fig. 5. First, the given geometric parameterization is checked to make sure the S-duct fits the assembly space. Next the S-duct geometry and the CFD-mesh are generated using DuctGen. Afterwards the visibility of the AIP is calculated in the visibility-tool. Then the CFD flow simulation is carried out in TRACE followed by post processing.

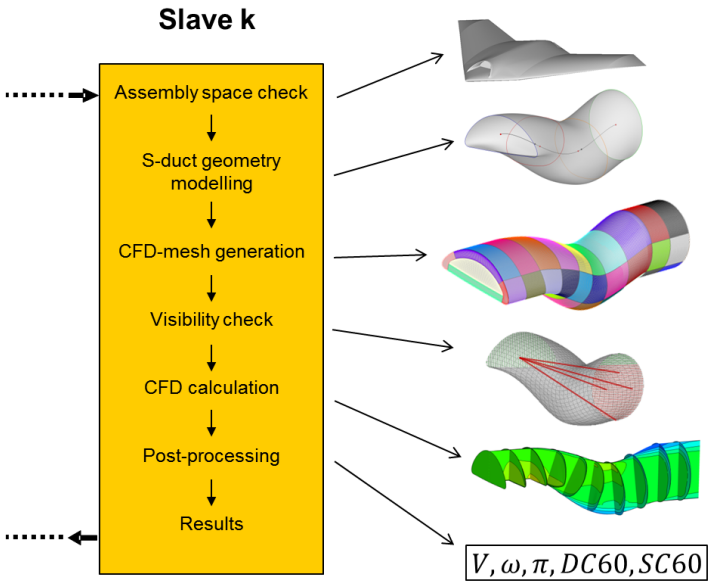

Fig. 5 Implemented process chain in *AutoOpti*.

F. Optimization settings

Parametrization: To optimize the S-duct in terms of flow characteristic and visibility, a geometric variation of the intake duct is necessary. Therefore different geometric parameters are set free, which can be seen in Fig. 6. In addition to a given and unchanged parametrization of the inlet and outlet rib-curves which are fixed due to the given UCAV (unmanned combat aerial vehicle) geometry and compressor constraints, there are three more rib-curves in between (Fig. 6, left). Each of these three rib-curves can be varied with five control points as shown in Fig. 6 (right). Four of these control points can be changed along the z-direction and one in the y-direction. A z-axis symmetry is enforced for all of the rib-curves. As seen in Fig. 6 (left) each rib-curve between the inlet panel and the outlet panel can be downscaled (yellow) and shifted along the spine-curve (green). Moreover, each rib-curve is shiftable in z-direction (orange) except the inlet rib-curve. Additionally the direction vectors at the inlet and the outlet are extentable to bend the S-duct flatter or steeper (red). In total, 27 free variables result from the selected geometric parameterization.

Objectives and constraints: For the optimization process a quantitative assessment of each generated S-duct geometry is necessary. One main task of the intake duct is to provide a stable, low-loss and homogeneous flow to the compressor. To quantify total pressure losses in the intake duct the total pressure loss coefficient

$$\omega = \frac{p_{t1} - p_{t2}}{\rho c_1^2/2} \tag{2}$$

is used. It determines the difference between the total pressure at the intake duct entry and exit, in relation to the dynamic pressure at the entry. Another measure considered for the flow losses in the intake duct is the total pressure ratio

$$\pi = \frac{p_{t2}}{p_{t1}}. \tag{3}$$

The distortion coefficient $DC60$ is considered as flow homogeneity in the S-duct outlet panel. For an efficient operation of the compressor a homogeneous total pressure distribution is beneficial [4]. The distortion coefficient is calculated comparing the averaged total pressure $p_{t,m}$ in the AIP with the minimal total pressure $p_{t,60,min}$ in a 60°-segment, normalized by the averaged dynamic pressure of the S-duct intake [15].

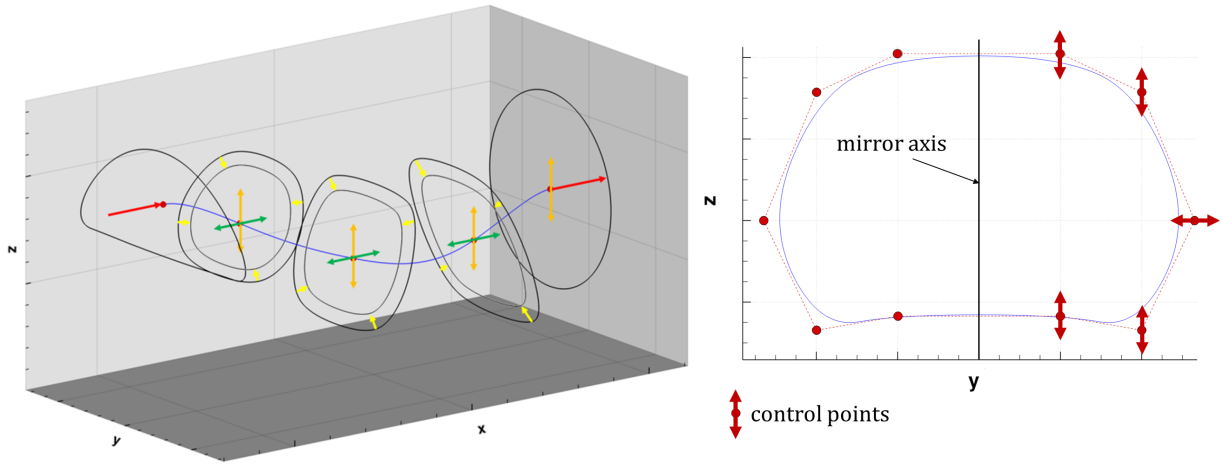

Fig. 6 Visualization of all free geometrical parameters of the S-duct structure (left) and the rib-curves (right).

$$DC60 = \frac{|p_{t,m} - p_{t,60,min}|}{\rho c_1^2/2} \tag{4}$$

Similar to the distortion coefficient the swirl distortion coefficient $SC60$ is considered for evaluation of flow uniformity. Therein the largest axial velocity deviation in a 60°-segment is put in relation to the absolute averaged axial velocity [16]:

$$SC60 = \frac{u_{max,60}}{u_{abs,AIP}}. \tag{5}$$

With this definition the swirl distortion coefficient considers rotation in the flow of the AIP and thus gives a statement about a possible swirl formation [16].

To summarize, the objectives are defined as follows:

$f_1 = V$

$f_2 = \omega$

IV. Results

This section presents the results of the optimization process. To ensure the functionality of the process chain and a high process chain convergence rate, a preliminary optimization study was carried out. A very simple parametrization of the S-duct was chosen (without rib-curve parametrization, see Fig. 6, left) and global improvements were achieved compared to the initial S-duct geometry. However, a significant reduction in the AIP-visibility could not be reached due to the simplified parametrization.

In the following, the global improvement based on the resulting Pareto front of the final optimization is presented. Based on this, a selection of auspicious configurations is made. Comparing these members, design features like visibility, the global flow field and the homogeneity in the AIP are presented.

A. Pareto front

With the convergence of 2525 members the optimization is aborted. Fig. 7 shows the Pareto front and all further converged members. The calculated objective function values of total pressure loss coefficient and visibility are plotted against each other. As can be seen from the Pareto front, a reduction in visibility leads to an increase in total pressure loss. It is marked whether a Pareto front member has a DC60 value and a SC60 value of less than 20 %. In addition, the Pareto front of the preliminary optimization series is shown for comparison purposes. Compared to the initial member used in this optimization, visibility and total pressure loss are significantly reduced. In addition, compared to the preliminary optimization, improvements in the total pressure loss coefficient are achieved for each percentage size of visibility that the former optimization could reach.

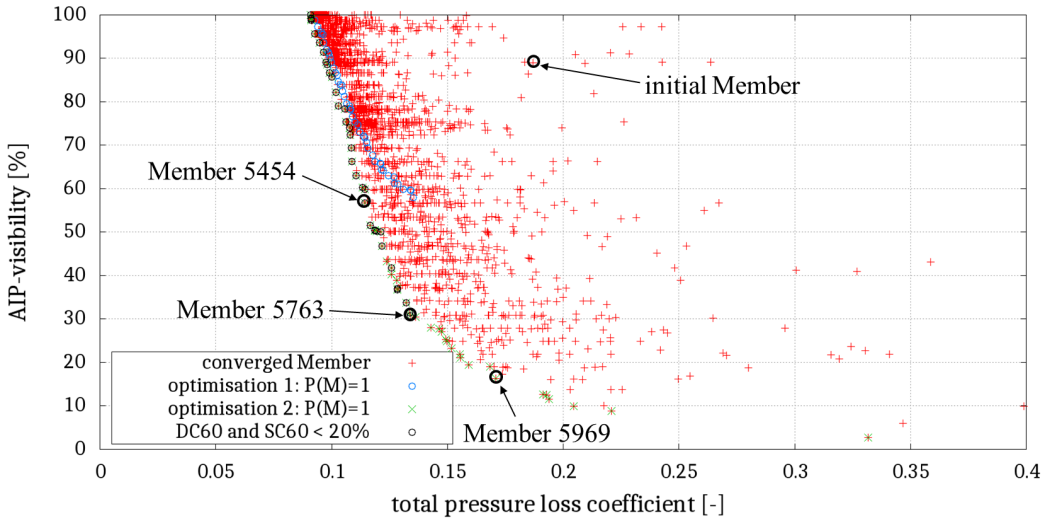

Fig. 7 Final Pareto front.

As seen in Fig. 7 the absolute minimum of visibility can be reduced down to 2.68 %. Since the flow losses for these members increase drastically up to a total pressure loss coefficient of 33.17 %, they are not considered for a detailed analysis. The losses in this low visibility area of the Pareto front are induced by shocks occurring in the S-duct. Member 5969 with a visibility of 16.32 % and a total pressure loss coefficient of 17.10 % is an alternative S-duct geometry concerning low visibility values and tolerable losses.

For the preselection of members with a likely homogeneous inflow in the AIP, those with comparatively low values for DC60 and SC60 are used for further analysis. Taking into account the members marked in Fig. 7 with a DC60 value and SC60 value below 20 %, Member 5454 and Member 5763 are selected. Compared to the preliminary optimization, Member 5763 has approximately 27 % lower visibility. To evaluate a reduction of the total pressure loss coefficient due to the new parameterization, Member 5454 is selected, which has a comparably low visibility of 56.69 % as the best members of the preliminary optimization with a total pressure loss coefficient that is approximately 2 % lower. In summary, the final selection of the members to be examined in this chapter is shown in Table 1, including the calculated assessment criteria.

Table 1 Resulting objectives and flowparameters.

Member	V	ω	π	$DC60$	$SC60$
5454	56.69 %	11.45 %	97.49 %	7.45 %	9.80 %
5763	31.44 %	13.37 %	97.09 %	14.12 %	17.28 %
5969	16.32 %	17.10 %	96.23 %	48.48 %	31.50 %

B. Visibility of the aerodynamic interface plane

As can be seen in Fig. 8 (left), a first factor to reduce the AIP-visibility is the distance between the spine-curve's maximum and minimum. The lower the minimum and the higher the maximum at the S-duct exit, the lower the visibility. For further analysis, the rib-curves are shown in Fig. 9. With the placement of the rib-curves orthogonal to the spine-curve, the free rib-curve parametrization allows an adaption to the exit contour of the AIP. This allows flatter but wider rib-curves in the spine-curve minimum. Thus, the lowest point of the S-duct upper side, as a combination of spine-curve and rib-curve progression, is mainly responsible for the AIP-visibility. Hence the lower AIP-visibility of Member 5969 compared to Member 5763 or Member 5454.

Another influencing factor is the cross-sectional area distribution as shown in Fig. 8 (right). All members show an increasing area distribution, which is determined by the fixed rib-curves at entry and exit. First, the area is expanded to

a maximum at a relative length of 25 %. The following minimum reduces the AIP-visibility by locally reducing the area to be viewed through.

In the case of Member 5763 and Member 5969, a second large maximum at 70 % relative length is evident. This point corresponds to the area of the spine curve's minimum of Member 5763 and Member 5969, so that the area is expanded at the lowest S-duct height. The following local minimum in the cross-sectional area distribution also reduces the AIP-visibility. This prevents an increase in the visibility of the AIP.

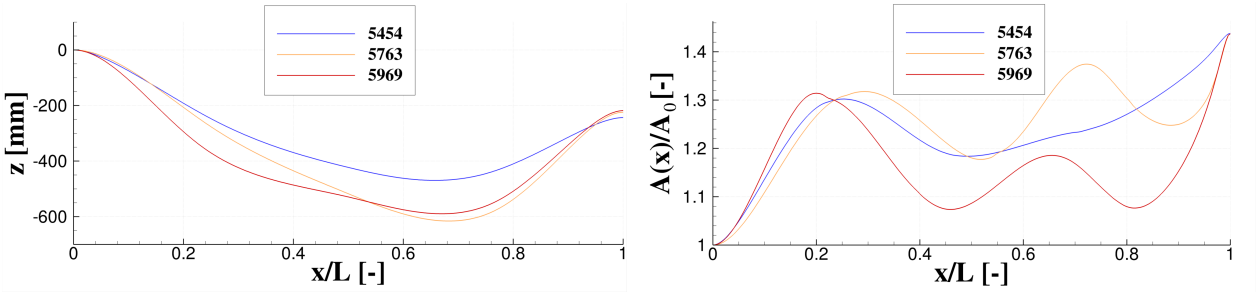

Fig. 8 Spine-curve progression (left) and area distribution (right).

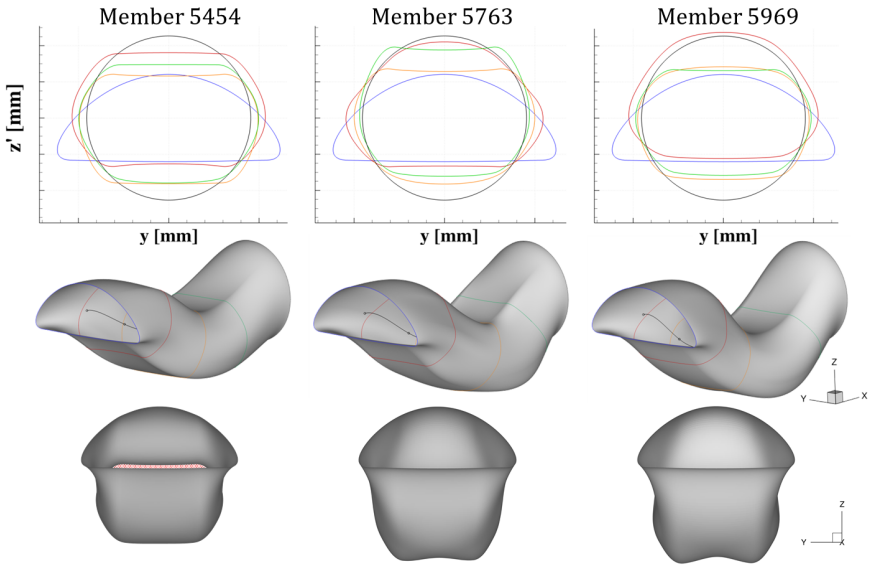

Fig. 9 Rib-curve coordinates (top), generated S-ducts (middle) and direct front view on S-ducts (bottom).

In a direct front view of Member 5454 the AIP is visible (see Fig. 9, bottom left), whereas the S-ducts of Member 5763 and Member 5969 hide the AIP.

Table 2 shows the minimum and maximum inclination γ of the UCAV under which the AIP is visible with the respective S-duct. With Member 5763 and a slight inclination of the aircraft of $-2.8°$, a visibility to the AIP already exists. For Member 5969, visibility is expected at an inclination angle γ between $-6.3°$ and $-16.6°$. In all other cases the AIP remains hidden from the outside. The absolutely visible inclination area $\Delta\gamma$ of member 5969 is the smallest with 10.3°.

C. Flow field analysis

In Fig. 10 (left) the flow fields of the three members selected from the Pareto front are compared by the Mach number development. In this figure, a main flow with low losses can be observed for all members. Due to the area expansion between inlet and outlet, the inflow Mach number is reduced. This causes an increase in static pressure in

Member	γ_{min}	γ_{max}	$\Delta\gamma$
5454	−23.3°	1.4°	24.7°
5763	−20.9°	−2.8°	18.1°
5969	−16.6°	−6.3°	10.3°

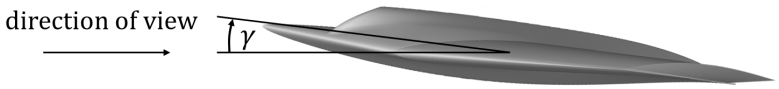

Table 2 Listing of the possible visibility of the AIP at minimum and maximum angle of inclination γ of the UCAV and the total visible inclination range $\Delta\gamma$.

flow direction. In addition, areas of large flow deflections are created as a result of sharper bending of the spine-curve necessary for a reduced visibility (figure 8, left). Thus, local Mach number maxima can be found at the lowest points of the S-duct topside. Behind these Mach number maxima areas of low-energy fluid compared to the main flow cause undesirable losses. The same effect can be seen at the lower side of the S-duct behind the local Mach number maximum near the inlet panel. In these areas the effect leads to cross-flow pressure gradients, which contribute to the formation of secondary flows and inhomogeneities of the local flow. The sharper bending of Member 5969 leads to larger areas of low-energy fluid at the upper side, than for the other members.

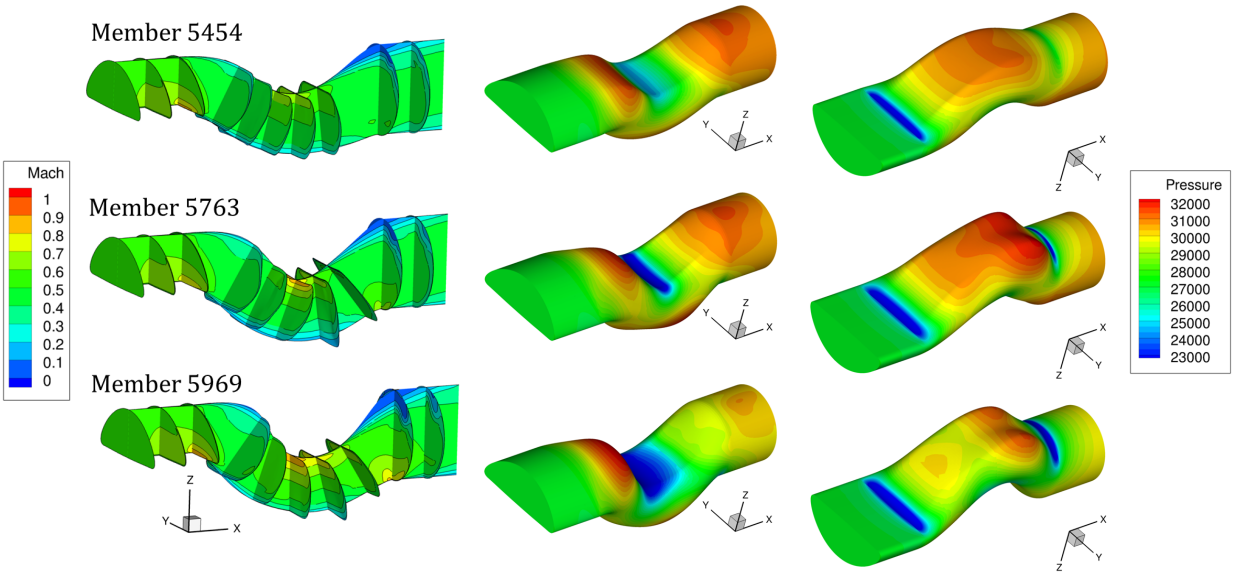

Fig. 10 Mach number contours (left) and wall pressure distribution on the upper side (middle) and the lower side (right) of the S-duct.

Fig. 10 (middle, right) shows the wall pressure distribution resulting from the flow deflections. As can be seen, the pressure ratio on the upper side in front of the AIP increases with the deflection in the middle of the S-duct. In addition, a high positive pressure gradient can lead to flow separation. To verify existing flow separations the wall shear stress can be seen in Fig. 11 (left). There is an area with negative wall shear stress in front of AIP for each considered member. Thus, the flow cannot follow the wall and high flow losses arise. As can be seen by the streamtraces in Fig. 11 (right), vortices are generated in this area which induce losses due to friction.

D. Flow uniformity in the aerodynamic interface plane

To assess the flow homogeneity, the total pressure loss coefficient of each selected member is visualized in Fig. 12 (left). Moreover the radial averaged total pressure over the circumferential angle φ is shown in this figure (right). Thus, loss-increasing areas can be observed at the upper side of the AIP. For example the total pressure of Member 5969 is reduced by approximately 2000 Pa in the area $\varphi \approx 60°$ compared to the mean value $p_{t2,m}$ in the AIP listed in Table 3. For Member 5763 and Member 5454 the total pressure deviations are comparatively small. They also show a more even distribution of the total pressure (see Fig. 12, right). In the area at the top of the AIP ($\varphi \approx 90°$) a total pressure recovery

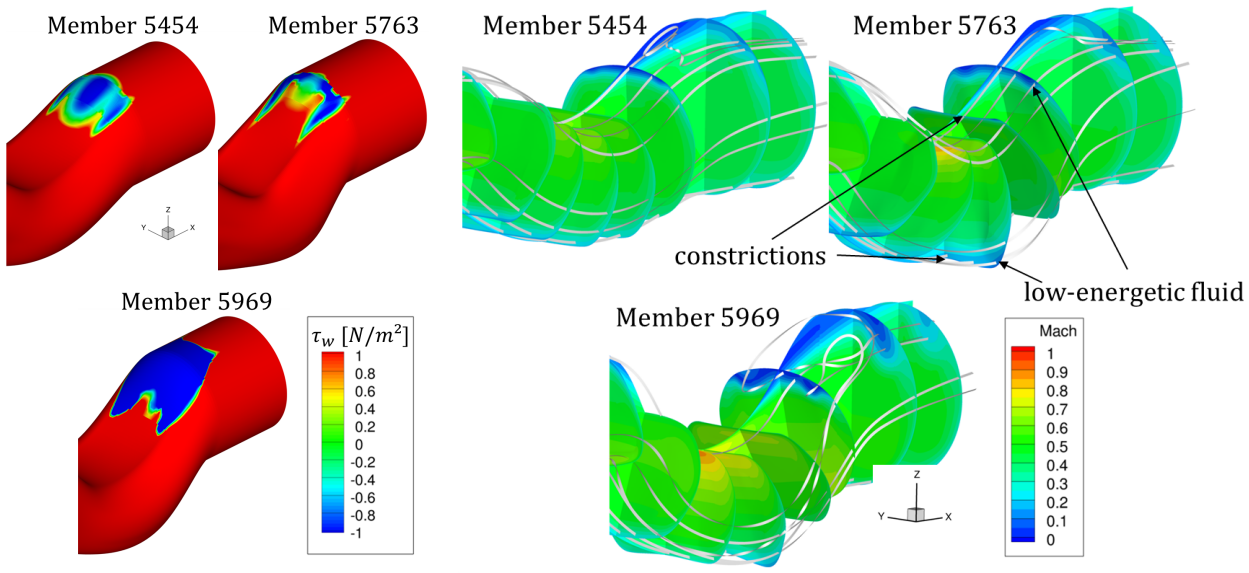

Fig. 11 Wall shear stress distribution (left) and streamtraces in Mach number contours (right) at the S-duct outlet area.

can be observed for all selected members. This behavior is caused by the symmetric vortices at $\varphi \approx 60°$ and $\varphi \approx 120°$. Moreover the total pressure distribution of Member 5969 is not symmetric due to a non-uniform overlap of cells at the zonal interface between the inlet extrusion block and the center block (see Fig. 10). Fig. 13 shows that the vortex centers have the lowest axial velocity and the highest losses due to high friction. Member 5969 has the lowest axial velocity due to the large vortex formation and backflow into the duct.

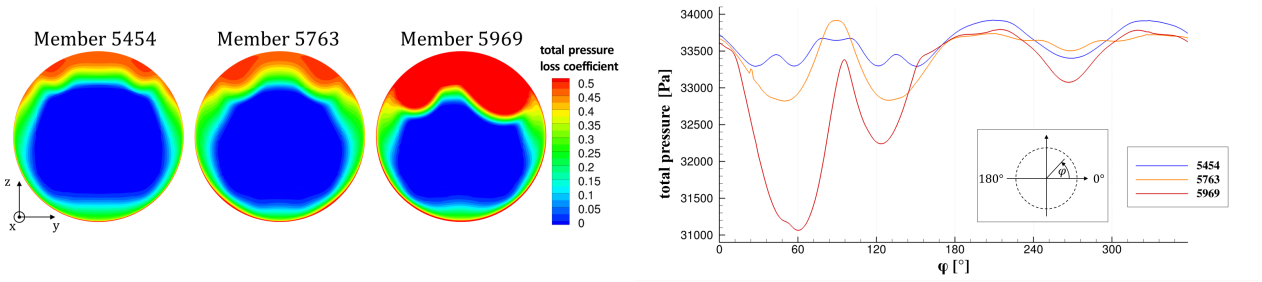

Fig. 12 Local total pressure loss coefficient (left) and radially averaged total pressure in circumferential direction (right).

As can be seen from the flow vectors in the AIP in Fig. 13 (left), the uneven axial velocity u generates a swirl that induces turbulence and results in losses due to friction. This vortex generation can be captured by the SC60 value, which is relatively high for member 5969 with 31.5 % (see Table 3). For Member 5763, due to a SC60 value of 17.3 %, a smaller vortex formation is to be expected, and for Member 5454 with 9.8 %, the lowest. This can also be derived from the circumferential velocity distribution in Fig. 13 (right). The radial averaged axial flow velocity of Member 5969 differs the most from the mean value.

Member 5454 and Member 5763 have low-energy fluid in the upper AIP. However, the flow velocity is not negative, which means that there is no backflow area in the AIP for Member 5454 and Member 5763 (see Fig. 13, left). A detailed analysis of the flow shows that for Member 5969 a distinct area of negative flow velocity u exists, which covers up a large part of the entire AIP.

Fig. 13 (left) illustrates an existing vortex in the AIP plane and the dominance of velocity in the z direction over velocity in the y direction which is caused by the flow deflection at the outlet panel, in front of the AIP. Accordingly, inhomogeneities increase with a reduction in visibility.

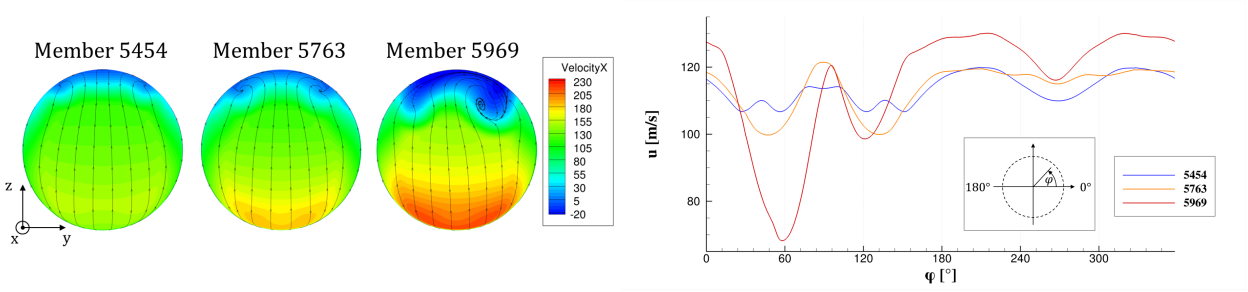

Fig. 13 Local axial velocity in x direction (left) and radially averaged axial velocity u in circumferential direction (right).

Member	$DC60$	$p_{t2,m}$ $[Pa]$	$SC60$	$u_{abs,AIP}$ $[m/s]$
5454	7.45 %	33610	9.8 %	113.8
5763	14.12 %	33474	17.3 %	114.4
5969	48.48 %	33179	31.5 %	118.8

Table 3 $DC60$, $SC60$ and corresponding values of averaged total pressure and axial velocity in the AIP.

E. Final S-duct selection

Based on the results, a final design selection is made. Since the visibility of the AIP is crucially important for the survivability of the UCAV, an S-duct with low AIP-visibility must be selected. However, due to the limited assembly space, it is not possible to avoid the visibility of the AIP at all inclination angles. In addition, S-ducts with a visibility below 17 % cannot be taken into account, due to high losses.

Thus, the most suitable S-ducts are those, that hide the AIP in a direct front view on the UCAV. Moreover, the inclination range has to be as small as possible. Member 5763 and Member 5969 meet these criteria. Further selection is made taking the numerical flow solutions into account. Thus, the calculated flow losses have to be tolerable and a homogeneous flow to the AIP has to be given. In view of these criteria, Member 5969 can not guarantee the efficient and safe operation of the engine.

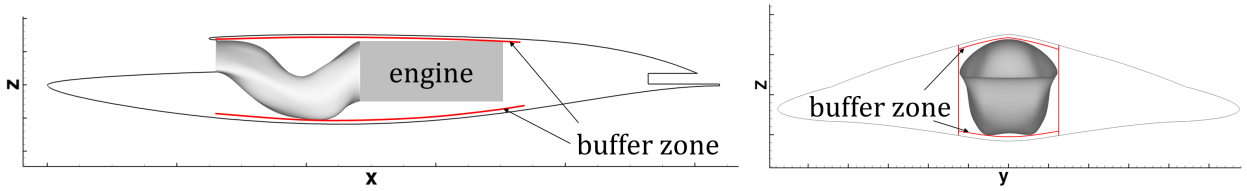

Fig. 14 UCAV-space in a side view (left) and a front view (right).

Since a total pressure loss coefficient of about 13 % is tolerated to ensure the survivability of the UCAV, the S-duct resulting from Member 5763 with a visibility of 31.44 % is a an appropriate choice. A developed main flow with a high total pressure recovery at the compressor inlet can be provided with that member. Thus, the S-duct generated from Member 5763 is selected as the final design for the UCAV .

V. Conclusion and future work

With the optimization process presented in this paper, various S-ducts with significantly reduced losses, AIP-visibility and homogeneity criteria could be created. Underneath an AIP-visibility lower than approximatively 17 %, the fluid mechanical losses caused by shocks and separations are to high to ensure an efficient engine operation. Above this value, acceptable S-ducts were chosen for analysis. With the 27 free parameters it was possible to reduce the visibility by adjusting the rib-curve contour to the S-duct outlet contour. In addition, high flow deceleration is avoided due to cross-section expansion. In this way the formation of flow separation areas is reduced. An overall reduction in the

visibility of the AIP and the flow losses is achieved. Finally, S-ducts were generated that do not allow a front view on the AIP. However, concealment was not achieved with the parameterization setup and the available assembly space.

Based on the results, a final S-duct for integration into the UCAV could be determined. This S-duct has a small area of low-energetic fluid at the upper side of the AIP which results in flow losses. However, these losses must be tolerated with regard to the survivability of the aircraft. Finally the S-duct has an AIP visibility of 31.44 % and a total pressure loss coefficient of 13.37 %.

In addition to the presented results, further investigations should be carried out. It remains to be investigated whether a reliable engine inflow at other operating points can be guaranteed with the selected S-duct.

In further investigations a larger assembly space for completely reducing the AIP-visibility should be considered. Furthermore the aircraft structure in front of the S-duct should be taken into account. The use of further rib-curve parameters can lead to an additional potential for minimizing the AIP-visibility. In addition, the size of the selected buffer zones (see Fig. 14) should be verified by taking infrared emissions through engine heat transfer into account.

References

[1] Torenbeek, E., *Advanced Aircraft Design: Conceptual Design, Technology and Optimization of Subsonic Civil Airplanes*, John Wiley and Sons, 2013.

[2] Howe, D., "Introduction to the Basic Technology of Stealth Aircraft: Part 1 - Basic Considerations and Aircraft Self-emitted Signals," ASME, Cranfield Institute of Technology, Bedford, England, 1990.

[3] Howe, D., "Introduction to the Basic Technology of Stealth Aircraft: Part 2 - Illumination By the Enemy," ASME, Cranfield Institute of Technology, Bedford, England, 1990. doi:10.1115/1.2906534.

[4] Seddon, J., and Goldsmith, E., *Intake Aerodynamics - Second Edition*, AIAA Education Series, Reston, Virginia, 1999. doi:10.2514/4.473616.

[5] Cummings, R. M., Liersch, C. M., Schütte, A., and Huber, K. C., "Aerodynamics and Conceptual Design Studies on an Unmanned Combat Aerial Vehicle Configuration," Journal of Aircraft, 2016. doi:10.2514/1.C033808.

[6] Becker, K., Heitkamp, K., and Kügeler, E., "Recent Progress In A Hybrid-Grid CFD Solver For Turbomachinery Flows," *Proceedings Fifth European Conference on Computational Fluid Dynamics ECCOMAS CFD 2010. V European Conference on Computational Fluid Dynamics ECCOMAS CFD 2010*, 2010.

[7] Voß, C., "Behandlung von Unsicherheiten in der Ersatzmodell gestützten Optimierung," Probalistik Workshop, Dresden, 2012.

[8] Aulich, M., and Siller, U., "High-dimensional constrained multi-objective optimization of a fan stage," ASME Turbo Expo, Canada, 2011.

[9] Voß, C., and Nicke, E., "Automatische Optimierung von Verdichterschaufeln. Abschlussbericht zum AG-Turbo COOREFF-T Teilvorhaben 1.1.1 des Verbundprojektes „CO2-Reduktion durch Effizienz"," 2008.

[10] Siller, U., Voß, C., and Nicke, E., "Automated Multidisciplinary Optimization of a Transonic Axial Compressor," Proceedings of the 47th AIAA Aerospace Sciences Meeting Including the New Horizons Forum and Aerospace Exposition, Köln, 2009.

[11] Voß, C., Aulich, M., and Raitor, T., "Metamodel Assisted Aeromechanical Optimization of a Transonic Centrifugal Compressor," ISROMAC, Honolulu, USA, 2014.

[12] Voß, C., Aulich, M., and Raitor, T., "Optimization Strategies demonstrated on a Transonic Centrifugel Compressor," ISROMAC, Honolulu, USA, 2014.

[13] Siller, U., and Voß, C., "Automated Optimization of a Double S-Shaped Inlet for Minimum Loss and Reduced Sight onto the Engine Face," *The 13th International Symposium on Transport Phenomena and Dynamics of Rotating Machinery*, ISROMAC, Honolulu, Hawaii, 2010.

[14] Wilcox, D. C., "Formulation of the k-ω Turbulence Model Revisited," AIAA, DCW Industries, Inc., La Cañada, California, 2008. doi:10.2514/1.36541.

[15] Çağlar Atalayer, Friedrichs, J., and Wulff, D., "S-Duct Intake Configuration Sensitivity of a Highly Loaded Turboprop by CFD Methods," *Proceedings of ASME Turbo Expo 2015: Turbine Technical Conference and Exposition*, ASME, Montreal, Canada, 2015. doi:10.1115/GT2015-42932.

[16] Taskinoglu, E. S., Jovanovic, V., and Knight, D. D., "Design Optimization for Submerged Inlets - Part II," *21st Applied Aerodynamics Conference*, AIAA, Orlando, Florida, 2003. doi:10.2514/6.2003-3926.